Fluid modeling of void closure in microgravity noble gas complex plasmas

Victor Land,* Lorin S. Matthews, and Truell W. Hyde
Center for Astrophysics, Space Physics and Engineering Research, Baylor University, Waco, Texas 76798, USA

Diana Bolser
The University of Missouri, Missouri, USA

(Received 1 February 2010; revised manuscript received 25 March 2010; published 12 May 2010)

A self-consistent dusty plasma fluid model has been extended to incorporate all the noble gases as the carrier gas. An analysis of void closure in complex plasma composed of these gases over a wide range of experimental parameters is presented. Driving potential-pressure maps are constructed, which show the range in parameter space where isotropic void-free dust crystals can be expected, where a void is to be expected and where the discharge is expected to extinguish.

DOI: 10.1103/PhysRevE.81.056402 PACS number(s): 52.25.Fi, 52.27.Lw, 52.30.Ex, 52.65.Kj

I. INTRODUCTION

The Coulomb crystallization of small solid particles embedded in plasma was realized in the laboratory some 15 years ago [1–4]. Ever since, *dusty* or *complex* plasmas have been used to study many phenomena from solid state physics, including diffusion and superdiffusion [5], waves [6], shocks [7], and phase transitions [8] on a scale accessible with ordinary optical techniques.

In the laboratory, gravity confines these systems to two dimensions. However, within 5 years of their discovery, dusty plasma experiments were conducted on board of sounding rockets, allowing second- to minute-long microgravity experiments [9]. Within a decade, these experiments were put aboard space stations orbiting earth, first Mir [10] and later the International Space Station [11], allowing microgravity experiments to be run for much longer times. One of the goals was to obtain large, three-dimensional, isotropic Coulomb crystals so that the aforementioned phenomena (and more) could be studied in three dimensions.

Instead, a phenomenon called *the void* appeared [12], which is a volume in the center of microgravity experiments, experiments utilizing thermophoresis [13], or containing very small particles (nanometer to submicrometer in size) [12], which expels dust particles and is therefore dust-free. Voids became topics of intense study, increasing the understanding of the ion drag force resulting from the interaction between flowing ions and solid particles [14]. The appearance of voids, however, opposed the initial concept of studying large, isotropic, three-dimensional dust crystals and in that sense constituted an unwanted by-product.

It was only recently experimentally shown how a void can be closed by reducing the power supplied to the dusty plasma [15]; even more recently, self-consistent numerical simulations showed that the same result can be obtained by changing the gas pressure [16]. Unfortunately, this self-consistent study only included argon as the carrier gas over a limited range of parameters, whereas current and planned experiments use both neon and krypton as the carrier gas [17], while xenon is a noble gas of interest for plasma propulsion schemes (such as Hall thrusters) due to its low ionization potential and high ion mass [18].

This work extends a numerical dusty plasma fluid code [19–22] by implementing all noble gases as the carrier gas. In this paper, we focus on the closure of dust-free voids in microgravity complex plasmas in helium, neon, argon, krypton, and xenon. In Sec. II, we discuss the model and outline how the different gases are implemented. Section III shows plasma solutions, while Sec. IV discusses void closure in these plasmas. Finally, Sec. V draws conclusions from our results and presents an outlook for future numerical studies of voids in noble gas dusty plasmas. Our primary goal is to present a roadmap for experimenters, showing at which driving potentials and pressures a microgravity noble gas complex plasma will contain a void or remains void-free.

II. MODEL

Modeling dusty plasma requires a solution to two difficult problems, namely, the coupling between the charged plasma particles and the imbedded dust particles (including their charging and transport), and the huge difference in time scales between the plasma particle motion and the dust particle motion. The fluid model discussed in this paper solves both these problems. In this section, we describe the method used, as well as the extensions applied to the model to implement the different noble gases.

A. Geometry

The geometry we consider in this paper is similar to the PKE/PK3-Plus geometry aboard the International Space Station. The dimensions are summarized in Fig. 1. Making use of the cylindrical symmetry of the devices, we model half of the plane shown in the figure to reduce computation time. A grid is superimposed on the plane, with a resolution of 48 (radial) by 96 (axial) grid points. The axial distribution of the grid points is not equidistant. The area between the electrodes contains two-thirds of the 96 total axial points, while the areas next to the electrodes both contain one-sixth. This means that the radial resolution in the model is 1 mm per

*victor_land@baylor.edu

 ©2010 The American Physical Society

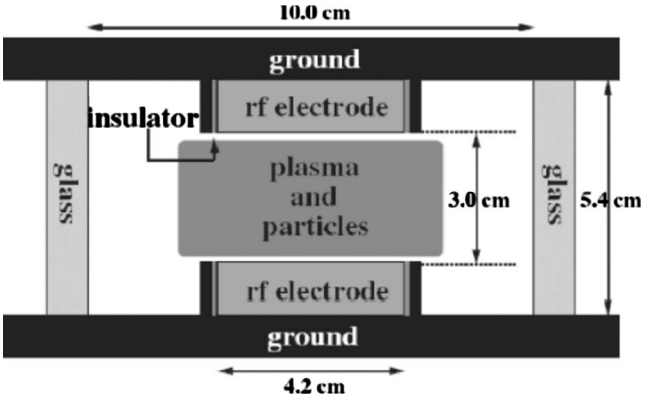

FIG. 1. Geometry in the model is similar to the PKE/PK3-Plus geometry. The dusty plasma solutions are obtained on a grid with a radial resolution of 1 mm/interval and an axial resolution of 0.75 mm/interval (next to the electrodes) or 0.47 mm/interval (in between the electrodes).

interval, while the axial resolution is as low as 0.47 mm per interval between the electrodes, but 0.75 mm next to the electrodes.

In the experiment, dust particles are introduced into the plasma using shakers (not shown in the figure) located in the electrodes. In order to model this, we use source terms just above the lower and just below the upper electrode. The equilibrium, periodic plasma solutions are obtained for points on the grid and these are then used to compute the dust transport.

B. Plasma solutions

The solution for the electrons and ions ($j=e$, $j=+$, respectively) is found by solving the continuity equation, while the momentum equation is replaced by a *drift-diffusion* equation for the particle flux, $\mathbf{\Gamma}_j$,

$$\frac{\partial n_j}{\partial t} + \nabla \cdot \mathbf{\Gamma}_j = S_j, \tag{1}$$

$$\mathbf{\Gamma}_j = n_j \mu_j \boldsymbol{E} - D_j \nabla n_j. \tag{2}$$

In the above equations, n_j is the number density, μ_j and D_j are the mobility and diffusion coefficients, respectively, and S_j the sources and sinks. The latter involve rate coefficients for several processes, in this case electron impact ionization and recombination of plasma on the dust.

The instantaneous electric field is obtained through the Poisson equation

$$\nabla^2 V = -\frac{e}{\epsilon_0}(n_+ - n_e - Z_d n_d), \tag{3}$$

$$\mathbf{E} = -\nabla V, \tag{4}$$

with Z_d the dust charge number and n_d the dust number density. The ions are too heavy to follow the instantaneous electric field, hence an effective electric field, $\boldsymbol{E}_{eff}$, is iteratively calculated from the instantaneous electric field [23]

$$\frac{\partial \boldsymbol{E}_{eff}}{\partial t} = \nu_m (\boldsymbol{E} - \boldsymbol{E}_{eff}), \tag{5}$$

with $\nu_m = e/m_+\mu_+$ the ion momentum transfer frequency.

The electron energy density ($w_e = n_e \epsilon$, with ϵ the mean electron energy) is solved with equations similar to Eqs. (1) and (2)

$$\frac{\partial w_e}{\partial t} + \nabla \cdot \mathbf{\Gamma}_w = -e\mathbf{\Gamma}_w \cdot \boldsymbol{E} + S_w, \tag{6}$$

$$\mathbf{\Gamma}_w = \frac{5}{3}(\mu_e w_e \boldsymbol{E} - D_e \nabla w_e). \tag{7}$$

Here, S_w represents the energy losses in inelastic collision processes and the losses due to recombination on the dust. The first term on the right-hand side of Eq. (6) corresponds to the Ohmic heating of the electrons in the instantaneous electric field. Most of the resulting electron energy is lost in inelastic collisions with neutral atoms; only during a short time period each rf cycle is electron energy lost to the walls. In the model, the ions are assumed to collide with background neutral atoms so frequently that their energy is locally dissipated to the background gas. The above set of equations is solved on sub-rf time scales allowing the electrons to be followed in the instantaneous electric field.

C. Electron collision rate coefficients

The behavior of the plasma strongly depends on the sources and sinks of particles and electron energy. Hence, rate coefficients must be calculated in order to incorporate different gases in the model. This involves using a *Boltzmann solver*, which calculates the collision probability for electrons in the different gases, as a function of the *reduced electric field* E/N, using tables of atomic collision cross sections for different inelastic collision processes. We used the freely available BOLSIG+ program, as described in [24]. Rather than using the reduced electric field, we use the mean electron energy, which has been shown to be a better choice for the type of discharges under consideration [25]. The rate coefficients multiplied by the local electron density and the neutral gas density give the source terms: $S_j = n_e n_{gas} k_j$. Multiplying these by their corresponding threshold energy gives the energy source terms $S_{w,j} = S_j E_j$, providing the right-hand side of Eqs. (1) and (6).

Despite the above, some physics of rf discharges is not easily included in fluid models, such as the effect of secondary electron emission, but especially nonlocal effects. Electrons can have mean-free paths comparable to the size of the discharge, which means that their heating is no longer related to the local electric field. Hybrid approaches, such as discussed in [26], attempt to partially solve this issue by using a Monte Carlo plus particle-in-cell approach for these so-called *fast electrons*, while using the fluid model for the *cold electrons*. Even though such an approach is valuable, it does involve a somewhat arbitrary cutoff energy to determine in which category a certain electron belongs, plus a computationally expensive scheme that keeps track of electron ener-

TABLE I. Inelastic transitions included in BOLSIG+ for the computation of the rate coefficients (and the transport coefficients discussed below). Although these collisions are only a fraction of all collisions in the atom, they include the most likely transitions from the ground state. *Other* refers to several excited states in krypton around 11 eV taken as one state. The BOLSIG+ software comes with a comprehensive list of references.

Gas	Level ($1S_0\rightarrow$)	Threshold energy (eV)	Gas	Level ($1S_0\rightarrow$)	Threshold energy (eV)
Helium	$2S_3$	19.8	Neon	$1S_5$	16.62
	Ionization	24.6		$1S_4$	16.67
Argon	$1S_5$	11.5		$1S_2$	16.84
	Ionization	15.8		$2P_2$	18.72
Krypton	$1P_1$	9.5		$3D_2+3D_5$	20.0
	$3P_2$	10		$3P_i$ $(i=1-9)$	20.65
	$3P_1$	10		Ionization	21.56
	$3P_0$	10	Xenon	$1S_5$	8.31
	Other	11		$1S_4$	8.44
	Ionization	14		$2P_9+2P_6$	9.69
				$2P_5+3D_{(6-1)}+3D''$	10
				$2P_{(4-1)}$	11
				$(3S-9S)_{\text{allowed}}$	11.7
				Ionization	12.13

gies before and after collision events. Such an approach is beyond the scope of the current discussion.

The different inelastic collision processes are summarized in Table I. The notation used is the *Paschen* notation, where the first number indicates the main electron energy level, S, P, or D, indicates the sublevel, and the subscript involves the quantized angular momentum of the state (J).

D. Transport coefficients

The transport coefficients are needed to calculate the left-hand side of Eqs. (1) and (6). BOLSIG+ calculates these for the electrons, again as a function of E/N. Rather than calculating the transport coefficients on the grid as a function of mean electron energy, we simplified the calculation by using a fixed value for E/N of 100 Td (10^{-19} V m^2), which is a typical value for the electric field found in simulations [27] as well as in similar experiments [22]. Although this method is not exact, the transport coefficients vary slowly around $E/N\sim 100$ Td for the gases under consideration. The mean electron energy is also calculated by BOLSIG+, which can be compared to the mean electron energy found in our model, providing a check on the value of the reduced electric field.

The transport coefficients thus depend only on the gas number density. Using the ideal gas law, $P=Nk_BT_{gas}$, the gas density can be substituted in terms of pressure and temperature. It is customary to write the mobility μ (and similarly the diffusion coefficient, D) in terms of the standard mobility, μ_0, at one atmosphere and 273 K

$$\mu = \mu_0\left[\left(\frac{760}{P(\text{Torr})}\right)\left(\frac{T(\text{K})}{273}\right)\right], \tag{8}$$

however, in our model, we use the notation

$$\mu = \tilde{\mu}\left[\left(\frac{1000}{P(\text{mTorr})}\right)\left(\frac{T(\text{K})}{273}\right)\right], \tag{9}$$

so that $\tilde{\mu}=760\mu_0$, corresponding to the numbers presented in Table II.

A solver for ion transport coefficients is not readily available and one must resort to the literature. Unfortunately, experimental data are only available for a limited range of E/N at many different temperatures. Using several literature sources, summarized in the caption above Table II, ion-transport coefficients for experimental parameters close to our simulated discharge settings (thus, the expected $E/N\sim 100$ Td and temperature, $T_{gas}\sim 300$ K) were found. Recall that according to the Einstein relation, the mobility and diffusion coefficient are related as $D_+/\mu_+=k_BT_+/e$ for singly ionized atoms. Assuming the ion temperature is 300 K, this ratio becomes 0.025; hence the diffusion coefficients are expected to be much smaller than the mobility for the ions. For the electrons, T_+ has to be replaced with T_e, which is on the order of 10^4 K, so that the electron diffusion coefficient is larger than the mobility.

A complete list of the parameters is shown in Table II. It is obvious that the transport coefficients and computed mean energies decrease with increasing ion mass. Two parameters of particular importance for the computation of the background gas temperature profile are α and κ_T, the *accomodation coefficient* and *translational thermal conduction coefficient*, respectively.

E. Computation of the gas temperature profile

The background gas is mainly heated by ions dissipating the energy they gained through Ohmic heating to the neutral

TABLE II. Parameters used in the model to describe the different background gases. Electron mobilities and diffusion coefficients were obtained with BOLSIG+; ion mobilities and diffusion coefficients were found in [28–31]. Accommodation coefficients, α, were found in [32] and thermal conduction coefficients, κ_T, in [33]. The gas temperature was assumed to be $T_{gas}=300$ K, whereas the reduced electric field was assumed to be roughly $E/N\sim 100$ Td, where 1 Td$=10^{-21}$ V m^2. The average electron energy is calculated in BOLSIG+ and is added for comparison to model results.

	Helium	Neon	Argon	Krypton	Xenon
μ_e(m^2/Vs)	76	67	23	20	15
D_e(m^2/s)	728	743	204	154	94
$\mu_+(10^{-2}$ m^2/Vs)	81	22	16	6.5	4
$D_+(10^{-2}$ m^2/s)	2.1	0.42	0.11	0.16	0.104
α	0.923	0.912	0.893	0.954	0.95
$\kappa_T(10^{-3}$ W/Km)	151.3	49.1	17.7	9.43	5.65
$m_{ion}(10^{-26}$ kg)	0.669	3.37	6.69	13.99	21.925
$\langle\epsilon=3k_BT_e/2\rangle$ (eV)	14.7	13.5	6.9	5.6	4.4

atoms. Averaged over one rf cycle, this heating term is $H_{\mathrm{Ohm}}=e\langle\boldsymbol{\Gamma}_+\cdot\boldsymbol{E}\rangle$. In the presence of dust, atoms colliding with the dust can pick up part of the heat on the dust particle surface returning energy to the gas. We refer to this as thermal heat transfer to the gas and write this as $H_{th,d}$. This heat is conducted by the gas. The thermal balance for the gas averaged over one rf cycle then becomes

$$-\kappa_T\nabla^2T_{gas}=H_{th,d}+H_{\mathrm{Ohm}}. \tag{10}$$

To obtain $H_{th,d}$, the dust particle surface temperature is required. Recombination of ions and electrons on dust results in heating of the dust particle surface, whereas energy is lost through collisions with neutral atoms and blackbody radiation, H_{rad}. The recombination source term is given by

$$H_{rec}=n_dR_{rec}(E_{ion}-eV_d+\epsilon), \tag{11}$$

where the electron recombination rate R_{rec} is calculated from orbital motion limited (OML) theory (see below) as $R_{rec}=-I_e/e$, $-eV_d$ is the gain of ion energy in the sheath surrounding a dust particle with surface potential V_d ($V_d<0$, see below), and ϵ is the mean electron energy. The thermal heat transfer to the atoms is given by

$$H_{th,d}=\frac{\gamma+1}{16(\gamma-1)}\frac{P_{gas}}{\sqrt{T_{gas}}}\sqrt{\frac{8k_B}{\pi m_{gas}}}\alpha(T_d-T_{gas}), \tag{12}$$

while the black-body radiation loss is given by the Stefan-Boltzmann law

$$H_{rad}=\epsilon\sigma(T_d^4-T_{wall}^4). \tag{13}$$

In the above, γ is the ratio of specific heats, assumed to be 5/3 for all gases, ϵ is the emissivity of the dust particles, assumed to be 0.9 for melamine formaldehyde (MF) [33], and T_{wall} is the temperature of the walls surrounding the discharge, which in these simulations is fixed at room temperature. Equations (11)–(13) along with the balance for the gas are solved iteratively.

F. Dust solution

The dust is not a static component of a complex plasma, but is transported by a variety of forces. The main reason for this is that dust particles immersed in plasma collect electrons and ions from their surroundings, obtaining an electric charge in the process. At equilibrium, the charge is determined by the equality of the electron and ion current reaching the particles. These are calculated from OML theory [34] for a spherical particle with radius R,

$$I_e=-4\pi R^2en_e\sqrt{\frac{k_BT_e}{2\pi m_e}}\exp\left(\frac{eV_d}{k_BT_e}\right), \tag{14}$$

$$I_+=4\pi R^2en_+\sqrt{\frac{e_+}{2m_+}}\left[1-\frac{eV_d}{E_+}+0.1\left(\frac{eV_d}{E_+}\right)^2\frac{\lambda_D}{l_{\mathrm{mfp}}}\right]. \tag{15}$$

In the above equations, λ_D is the linearized Debye length, $l_{\mathrm{mfp}}=v_+/\nu_m$ is the mean-free path calculated at constant collision frequency, and $E_+=m_+v_+^2=4k_BT_{gas}/\pi+m_+u_+^2/2$, with u_+ the ion drift velocity calculated from the ion flux, Γ_+. The second term in square brackets in the ion current is an addition to OML theory due to charge-exchange collisions with neutrals, causing loss of ion energy and angular momentum and enhancing the ion current to the dust particle [35]. Using a Newton iteration to solve $I_e+I_+=0$ results in a solution for V_d. Assuming a simple capacitor model, the dust charge is found from $Q_d=eZ_d=V_d4\pi\epsilon_0R$. Due to the high electron mobility, a micron-sized particle carries thousands of electron charges, a charge that becomes more negative with increasing electron temperature.

Once the dust charge is calculated from the local plasma parameters, the forces acting on the dust are calculated. The force due to the time-averaged electric field $\langle\boldsymbol{E}\rangle$ is calculated as

$$\boldsymbol{F}_E=Q_d\langle\boldsymbol{E}\rangle. \tag{16}$$

The force due to the interaction between streaming ions and the dust particles, called the *ion drag*, is given by

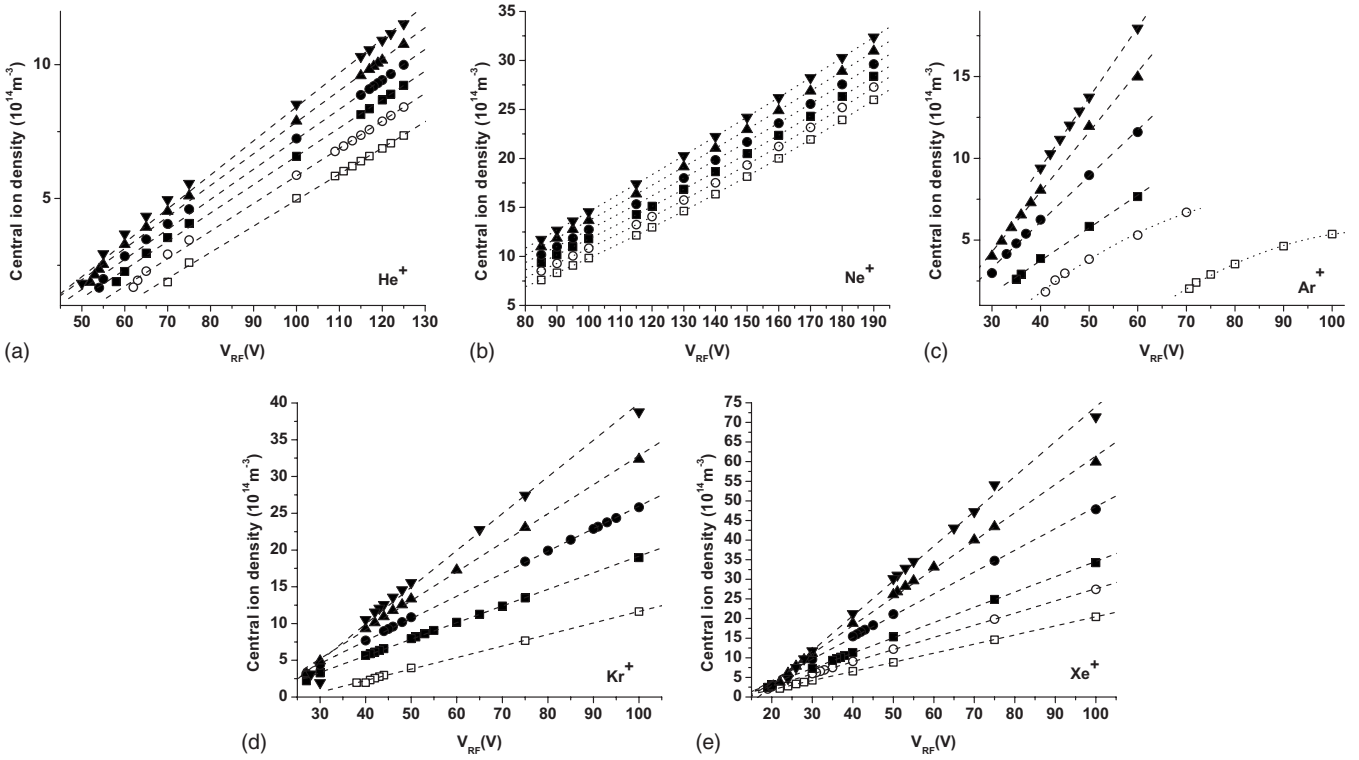

FIG. 2. Central ion densities obtained in the fluid model in units of 10^{14} m^{-3}. [(a) and (b)] For helium and neon, symbols refer to (□: 500 mTorr, ○: 550 mTorr, ■: 600 mTorr, ●: 650 mTorr, ▲: 700 mTorr, ▼: 750 mTorr). [(c)–(e)] For the other gases, symbols refer to (□: 100 mTorr, ○: 150 mTorr, ■: 200 mTorr, ●: 300 mTorr, ▲: 400 mTorr, ▼: 500 mTorr). Dashed lines are linear fits to the data points; dotted lines parabolic fits (used when linear fits were statistically insufficient). All shown fits have a level of confidence of at least R^2=0.99.

$$\boldsymbol{F}_{id} = n_+ m_+ v_+ \boldsymbol{u}_+ \times \left(\sigma_c + \pi \rho_C^2(v_+) \left[\Lambda(\tilde{v}_+) + \mathcal{K}\left(\frac{\lambda_D}{l_{\mathrm{mfp}}} \right) \right] \right). \tag{17}$$

Here, σ_c is the OML collection cross section for ions, $\rho_C(v_+)=Z_d e^2/2\pi\epsilon_0 m_+ v_+^2$ is the Coulomb radius, $\Lambda(\tilde{v}_+)$ is the Coulomb logarithm including scattering beyond the Debye length [14] calculated with an effective ion velocity (taking anisotropic screening due to ion drift into account [36]), and $\mathcal{K}(x)$ is a collision operator taking into account the increased ion flux due to charge-exchange collisions [37], similar to the increased ion current taken into account in the OML theory. The force due to gradients in the gas temperature profile, called *thermophoresis*, is calculated by

$$\boldsymbol{F}_{th} = -\frac{32}{15}\frac{R^2}{v_{th}} \kappa_T \nabla T_{gas}, \tag{18}$$

with $v_{th}=\sqrt{8k_B T_{gas}/\pi m_+}$ the mean thermal velocity of the background gas. Balance between these forces and neutral drag,

$$\boldsymbol{F}_n = -\frac{4}{3}\pi R^2 \rho_{gas} v_{th} \boldsymbol{v}_d, \tag{19}$$

results in an equation for the dust flux that can be integrated in time

$$\boldsymbol{\Gamma}_d = n_d (m_d \nu_{m,d})^{-1} [\boldsymbol{F}_E + \boldsymbol{F}_{id} + \boldsymbol{F}_{th}] - D_d \nabla n_d. \tag{20}$$

Here, the dust diffusion coefficient, D_d, depends on the coupling of the dust particles [38] and the dust-neutral momentum transfer frequency is given by $\nu_{m,d}=(\rho_{gas}/\rho_d)(v_{th}/R)$, with ρ_d the mass density of the dust particles (1510 kg m^{-3} for MF).

The plasma equations (1)–(7) are solved on sub-rf time scales. Once the solution has become periodic, a dust fluid is introduced into the discharge through the source terms and the forces are calculated on the grid. The dust flux is obtained through Eq. (20). Integrating this solution in time, the dust density is advanced using larger time steps. In order to maintain quasineutrality, the positive ions are moved with the dust. When this solution for the ion density deviates too much from the periodic solution, the dust is frozen and the iteration of the plasma solution is resumed on sub-rf time scales until convergence is reached again. This process is continued until the final equilibrium solution is found, with computed deviation from periodicity smaller than 1%.

III. PLASMA RESULTS

Figure 2 shows the central ion density as a function of pressure and driving potential for all the gases. Helium and neon were run in the pressure range of 500 mTorr $\leq P_{gas} \leq$ 750 mTorr, with the driving potential in the range 50 V $\leq V_{\mathrm{rf}} \leq$ 130 V for helium and 80 V $\leq V_{\mathrm{rf}} \leq$ 190 V for neon. Argon, krypton, and xenon were run at 100 mTorr $\leq P_{gas} \leq$ 500 mTorr, with 20 V $\leq V_{\mathrm{rf}} \leq$ 100 V.

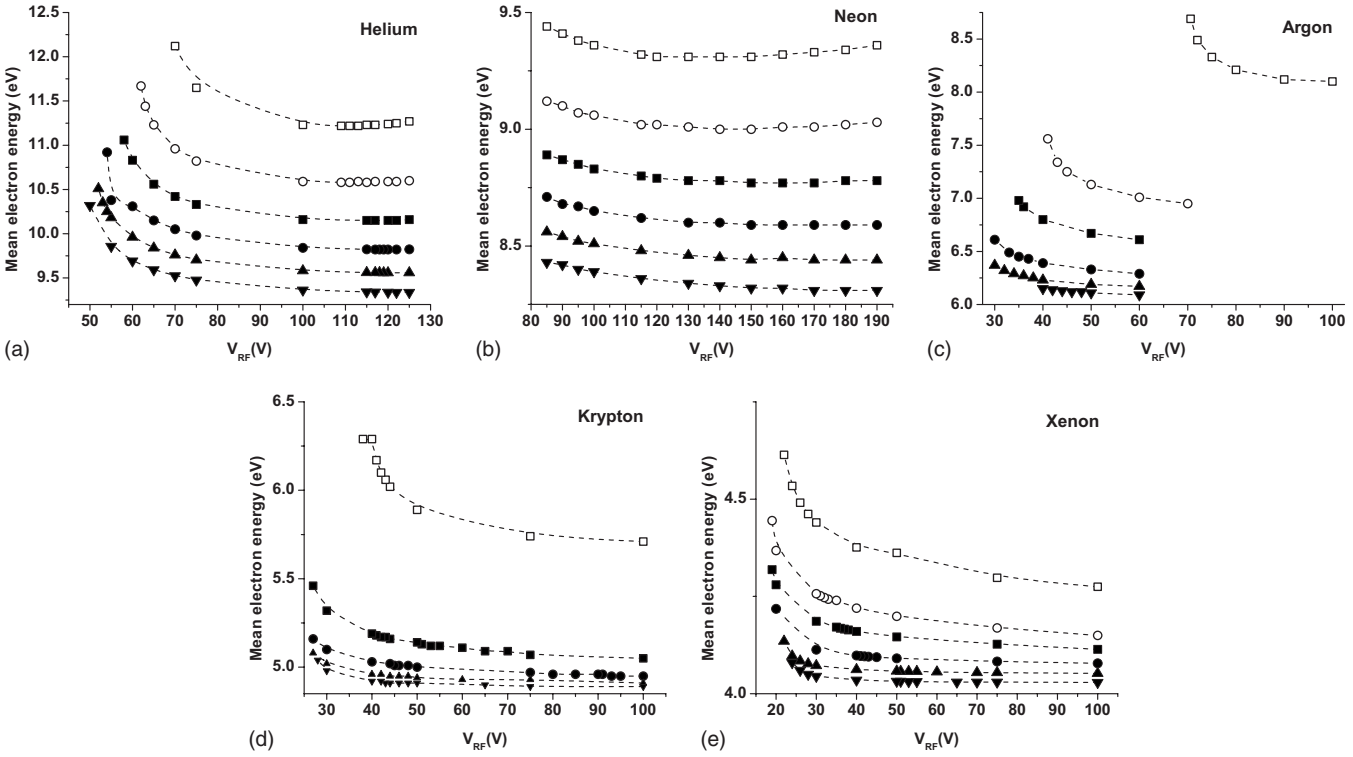

FIG. 3. Central mean electron energy, $\langle w_e \rangle = 3k_B T_e/2$, for the different gases obtained using the fluid model. For helium and neon, symbols refer to (□: 500 mTorr, ○: 550 mTorr, ■: 600 mTorr, ●: 650 mTorr, ▲: 700 mTorr, ▼: 750 mTorr). For the other gases, symbols refer to (□: 100 mTorr, ○: 150 mTorr, ■: 200 mTorr, ●: 300 mTorr, ▲: 400 mTorr, ▼: 500 mTorr). Dashed lines are added to guide the eyes.

The ion density increases with pressure and potential for all the gases, but the quantitative behavior of each gas is different. All gases but neon show a linear increase of the density with driving potential. In neon, this increase is quadratic. Argon is the only gas in our parameter range that showed extinction, namely, for the lowest two pressures. Close to extinction, the ion density no longer increases linearly with potential. The potential at which extinction occurs (V_x from now on) thus varies strongly in argon for the considered pressure range. For helium and neon, the point where the ion density vanishes (which should correspond to the point of extinction) also varies over a relatively wide range with pressure, whereas for krypton and xenon, the density vanishes almost at the same driving potential, showing that V_x is almost constant.

The results for the central mean electron energy are shown in Fig. 3. The electron temperature decreases with increasing pressure, consistent with previous simulations [22] and as explained in [39]. We also observe that the electrons cool with increasing driving potential, even though this cooling is very limited and might be hard to measure. For low driving potentials, there is a sudden increase in the electron temperature. Also, neon and helium show a slight increase in the electron temperature for high driving potentials, but again this change is small.

The mean electron energies obtained are roughly He: 11 eV, Ne: 9 eV, Ar: 7 eV, Kr: 5.3 eV, and Xe: 4.2 eV, while the values obtained with BOLSIG+ for $E/N \sim 100$ Td are He: 14.7 eV, Ne: 13.5 eV, Ar: 6.9 eV, Kr: 5.6 eV, and Xe: 4.4 eV. The values obtained for helium and neon are low compared to the BOLSIG+ values, which might indicate that the value of the reduced electric field in the fluid model is less than 100 Td in these gases. The values for the other three gases coincide well with the BOLSIG+ results, indicating that the effective electric field in our model is indeed close to 100 Td.

Overall, the ion density increases with decreasing ionization energy of the gas, while the electron temperature decreases. This intuitively makes sense, since electrons have to gain more energy to ionize helium than to ionize xenon. On the other hand, a smaller fraction of the electron population will be able to gain that much energy for a given reduced electric field. Therefore, higher ionization fraction coincides with lower mean electron energy.

Figures 4(a)–4(e) show the gas temperature at 500 mTorr for all the different gases at comparable driving potentials. The main source of heating of the gas is due to ions locally dissipating their energy to the gas. This means that the ion density plays an important role in the heating of the gas. Also, the conductivity of the gas determines whether or not the heat is contained within a volume close to where this dissipation occurs.

These two effects enhance each other. In helium and neon, the ion density is relatively low, so that little gas-heating occurs. Furthermore, κ_T is large in helium and neon, so that any heat produced can be effectively conducted away from the source. This leads to smaller temperature gradients. Increasing the ion density increases the temperature gradients in the gas, hence increasing the pressure and the driving

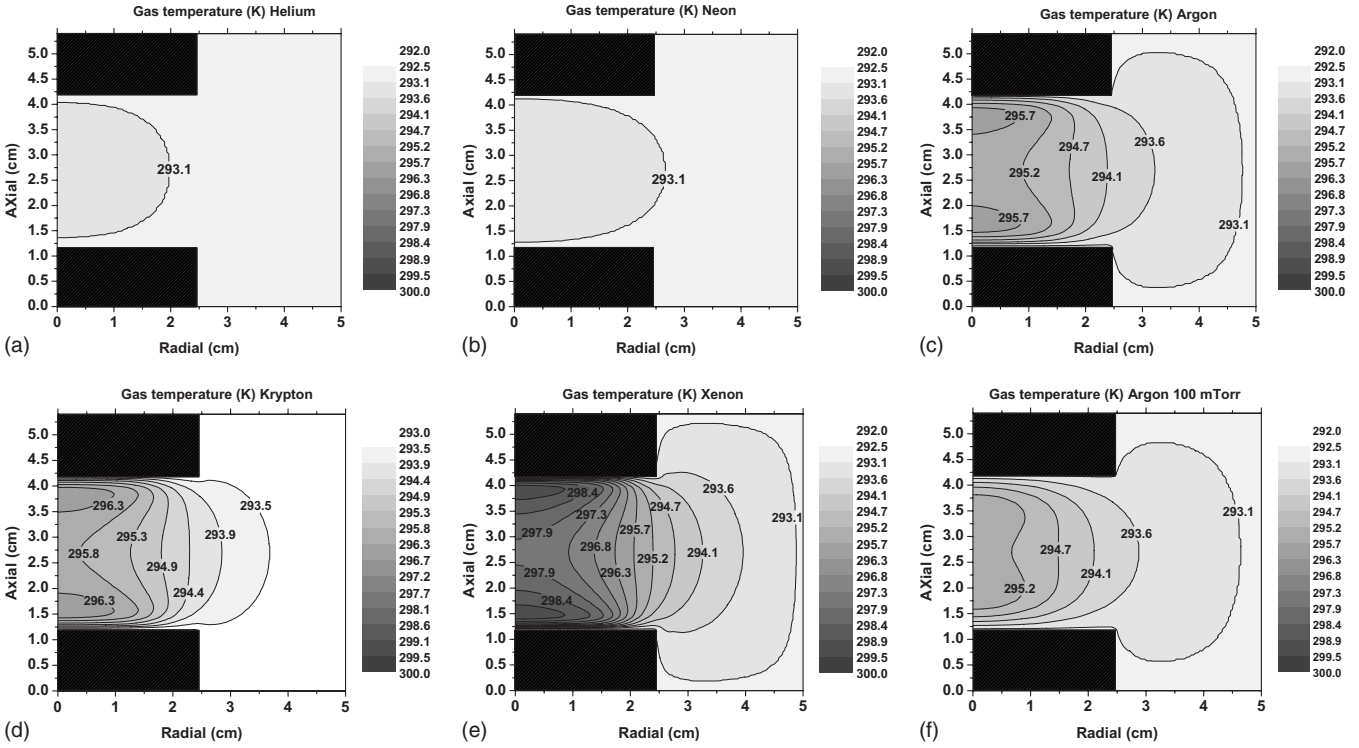

FIG. 4. Background gas-temperature profiles. The boundary temperature at the walls and electrodes was set at 293 K (room temperature). [(a)–(e)] Pressure of 500 mTorr at driving potentials of (a) 70 V, (b) 60 V, (c) 50 V, (d) 50 V, (e) 50 V, and (f) 50 V. Note the increasing temperatures and temperature gradients with decreasing thermal conduction coefficient. (f) The gas-temperature profile for argon at 100 mTorr and 50 V, with much smaller temperature gradients than in (c).

potential results in larger thermophoretic forces. Figure 4(f) shows the temperature profile in argon at a lower pressure of 100 mTorr. The lower ion-density results in less heat dissipation and the temperature gradients become much smaller, especially along the vertical axis.

In the radial direction, the temperature gradient is directed inwards, so that the thermophoretic force acts *against* void closure. In helium, neon, and argon, the temperature gradient along the vertical symmetry axis is small, but in krypton and xenon, the temperature gradient can become considerable. In the sheaths, close to the electrodes, the temperature gradient is directed inwards, away from the electrodes, so that the thermophoretic force is directed towards the electrodes. Toward the center, away from the sheaths, the gradient is directed outwards, toward the electrodes, so that the thermophoretic force acts *in favor of* void closure. We see that the dust particles initially have to move against this thermophoretic force after being released from dust dispensers built in the electrodes [11]. Once they pass the sheaths, the thermophoretic force helps them move inwards.

IV. VOID CLOSURE

We modeled void closure by adding 3.4 μm radius particles to the converged plasma discharges. No more than 10 000 particles were added, so that the effect of the dust on the discharge parameters is minimized and the main differences in void closure with varying discharge parameters can be contributed to the different gases. The local changes in the plasma parameters and gas-temperature profiles due to the dust are taken into account by the model. The void size is determined by the point where the net force acting on the particles vanishes. Since we are adding a relatively small number of particles, the pressures inside the dust cloud play only a small role in the position of the void edge, so we only have to consider the net external force. Furthermore, the quantitative behavior of the void size with varying driving potential in argon was shown to be similar for a much larger number of particles, only shifted to higher values of the driving potential [21].

We define the radial void size as the distance from the center of the discharge to that point located in the symmetry plane in between the electrodes where the net radial force vanishes (only one such point exists in our simulation domain, since we only model half of the $R-Z$ plane). Similarly, the axial void size is defined as the distance from the center of the discharge to the points on the rotational symmetry axis where the axial force vanishes (two such points exists in our simulation domain: one below and one above the center of the discharge). Figure 5 shows the radial and axial void sizes, R_v and Z_v, respectively, determined in this manner in argon and neon. For neon, the void was observed to close axially at the highest two pressures (700 and 750 mTorr) for all driving potentials considered in this paper. Therefore, these data points are not present in Fig. 5(d).

The first observation is that the radial void size is larger than the axial void size, both in argon (by a factor of two) and in neon (by a factor of 3). Secondly, the void tends to have a constant size for large driving potentials, but de-

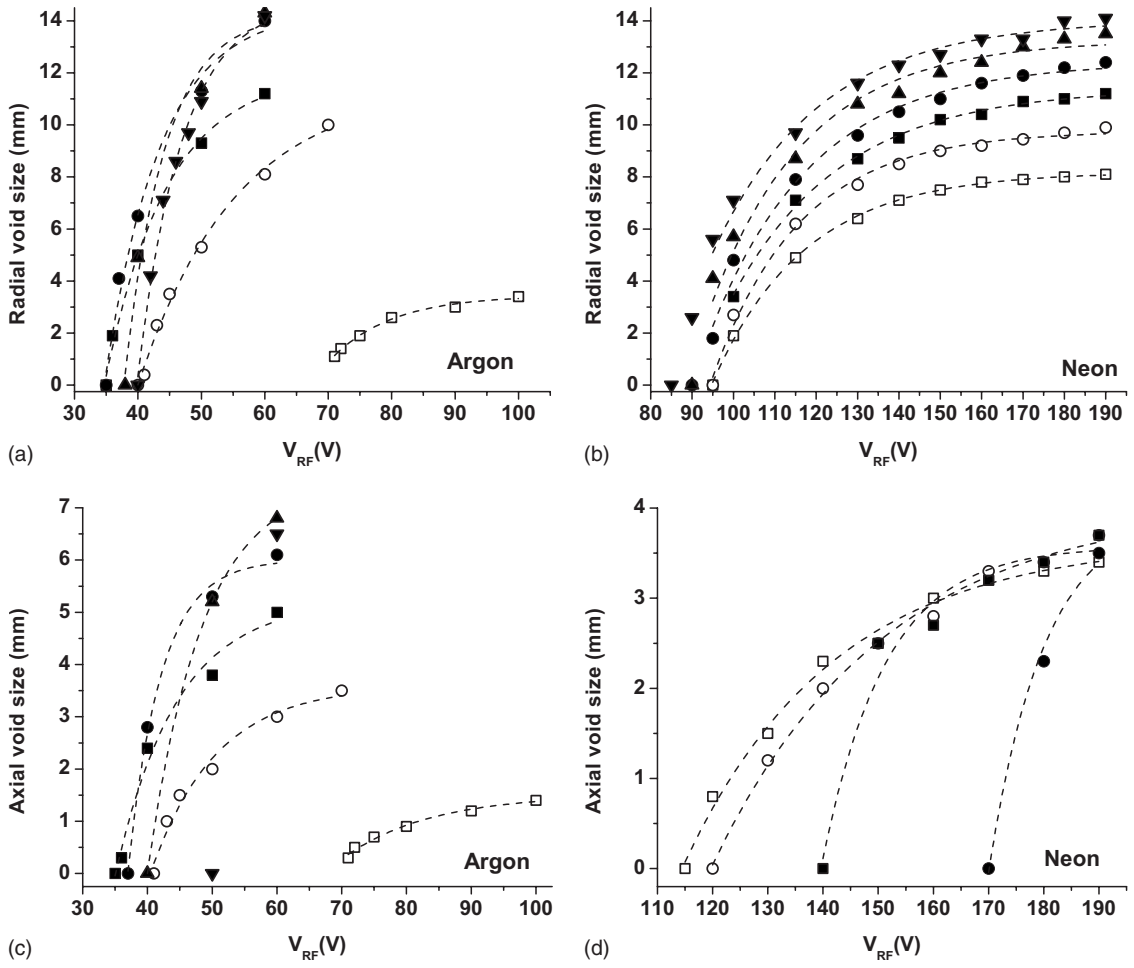

FIG. 5. [(a) and (b)] Radial and [(c) and (d)] axial void sizes for argon (left) and neon (right). For neon, the symbols refer to (□: 500 mTorr, ○: 550 mTorr, ■: 600 mTorr, ●: 650 mTorr, ▲: 700 mTorr, ▼: 750 mTorr); for argon to (□: 100 mTorr, ○: 150 mTorr, ■: 200 mTorr, ●: 300 mTorr, ▲: 400 mTorr, ▼: 500 mTorr). Dashed lines are fits according to Eq. (21), which all have a large statistical reliability, $R^2 > 0.98$.

creases suddenly with decreasing driving potential until closure occurs. Please note that for the lowest two pressures in argon (i.e. 100 and 150 mTorr), the plasma dies out before void closure can actually be achieved, even though this might not be completely obvious from Fig. 5.

In [15], void closure was experimentally measured for an argon discharge at 24 Pa using a large number of 3.4 micron radius MF particles. Even though the exact point of void closure was not shown, a driving potential of 18.3 V was mentioned. In [21], this experiment was simulated and void closure was found at 18.9 V without the effect of charge-exchange collisions and at 25 V with charge-exchange collisions, for a run with 130 000 dust particles. In our current model, a different set of transport coefficients is used, resulting in void closure for a similar pressure at 34 V. The shape of the void-closure curves obtained in experiment and simulations is similar, however.

Another important observation is that a change in discharge pressure does not significantly change the shape of the void-size curve, but mainly shifts it upwards. This is especially clear for the radial void size in neon. This gives the impression that all the lines in Fig. 5 should have the same dependence on the driving potential, but that each line has different prefactors that depend on the pressure. With this in mind, we produced a fit for the void size x_v (in both radial and axial direction) that is in remarkable agreement with the data points. The dashed lines in Fig. 5 are the fits to the data points given by

$$x_v(V_{\mathrm{rf}}, Pd) = a(Pd) - b(Pd)\exp\left(-\frac{V_{\mathrm{rf}}}{c(Pd)}\right). \qquad (21)$$

Rather than using just the pressure P, we used the pressure times the inter-electrode spacing, Pd, as the dependent variable, similar to the analysis done in determining breakdown voltages, or Paschen curves, in plasma discharges [39]. $a(Pd)$ is the void size at large driving potentials, which increases with Pd. $b(Pd)$ and $c(Pd)$ together determine the rate at which the void closes. These three variables of course depend on the carrier gas.

From Eq. (21), we can determine the driving potential at which the void closes $[V_0(Pd)]$ by setting $x_v = 0$. We obtain

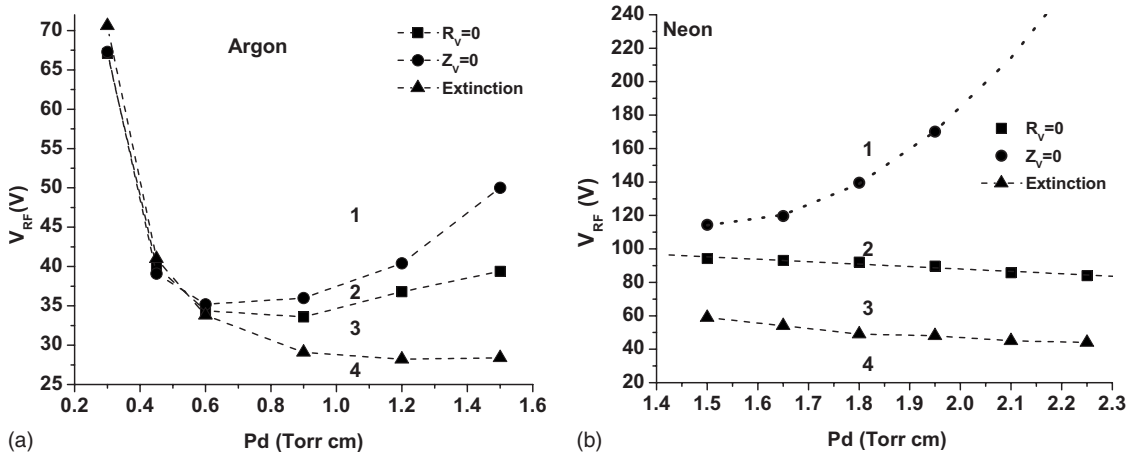

FIG. 6. Potentials for void closure from Eq. (22) and the extinction curve obtained for argon and neon. The differently labeled regions refer to (1) existence of a completely open void, (2) balance of the axial forces in the center, (3) balance of the axial and the radial forces in the center, hence the void closure, and (4) extinction of the plasma.

$$V_0(Pd) = \ln\left(\frac{b(Pd)}{a(Pd)}\right)c(Pd). \tag{22}$$

It is interesting that this equation looks somewhat similar to the original Paschen's law [40] for the breakdown voltage of a gas placed between two parallel charged plates. Note that we have two equations for the potential at which the void closes: one for each direction. The plots for V_0 are shown in Fig. 6 as a function of Pd together with the extinction curve determined with our model, i.e., the driving potential at which the plasma dies out.

Argon shows an interesting result; for low Pd, the extinction curve crosses both the axial as well as the radial curve for void closure, showing that the plasma dies out before void closure can be reached. With increasing Pd, the void closes both axially and radially for increasing driving potential, showing that it becomes increasingly *easier* to close the void. In neon, void closure could be achieved for all Pd values considered. It becomes *easier* to close the void axially, whereas it becomes slightly *harder* to close the void radially with increasing Pd. For the highest two pressures in neon, the axial void size vanished for all potentials considered in this study, which is also clear from the curve fit to the points at lower pressures. Since we did not consider driving potentials above 190 V, these points are not included in the graph.

It is clear that the three curves divide the $V_{rf}-Pd$ space into four *states*: (1) the plasma exists and the void has not closed in either of the two directions. (2) The plasma exists and the axial forces act such that particles would find balance in the plane between the two electrodes. However, the particles are still pushed radially outwards. Hence, a closed void can exist, but the dust pressure has to provide a significant inward radial force. (3) The plasma exists and the void has vanished both radially and axially. Here, a dust cloud is suspended in the discharge, while the dust pressure provides the outward force balanced by very small external forces. This would correspond to a three-dimensional, quasi-isotropic dust cloud, comparable to Yukawa or Coulomb balls in thermophoresis experiments [41]. (4) The plasma dies out. The discharge cannot be maintained in this part of the $V_{rf}-Pd$ space.

A slightly different graphical representation is used to show the modeled parameter space and the obtained *state* of the microgravity dusty plasma for all the gases considered (Fig. 7). The parameter-space maps look similar for all gases. The radial void closure line runs almost parallel to the extinction line, while the axial void closure potential increases rapidly with increasing Pd. Due to the extinction line, argon has a narrow V_{rf} range where the void should close, reopen, and then close again as Pd increases. Since the extinction curves are similar for all noble gases, it seems likely that this should happen for each gas, but simply at a much lower Pd value. In our model, helium and neon can only be simulated at much higher Pd values, as discussed below, and hence show a much broader range in V_{rf} where the void closes, which basically corresponds to the far-right side of the plots for the other gases. In the argon plot, data for the measured breakdown potential from [42] is added, which should be similar to our extinction curve. The absolute value of the breakdown potential is in reasonable agreement with the model, but the minimum occurs at a lower value of $Pd=0.4$ rather than $Pd=0.9$ in our model. It has to be noted that the data were obtained from a log-log plot and that the indicated error, due to manually selecting data from a log-log plot, probably underestimates the error in the experiment, which was not stated.

V. DISCUSSION AND CONCLUSION

The state maps for complex noble-gas plasmas under microgravity conditions (Fig. 7) are similar for all gases. In these maps, the state is determined by three curves. These curves are rather stable due to the large increase of the ion drag force and electrostatic force for a small change in discharge parameters. For instance, the difference between the appearance of a void and void closure is as small as 0.5 V for the driving potential, whereas the extinction curve is even

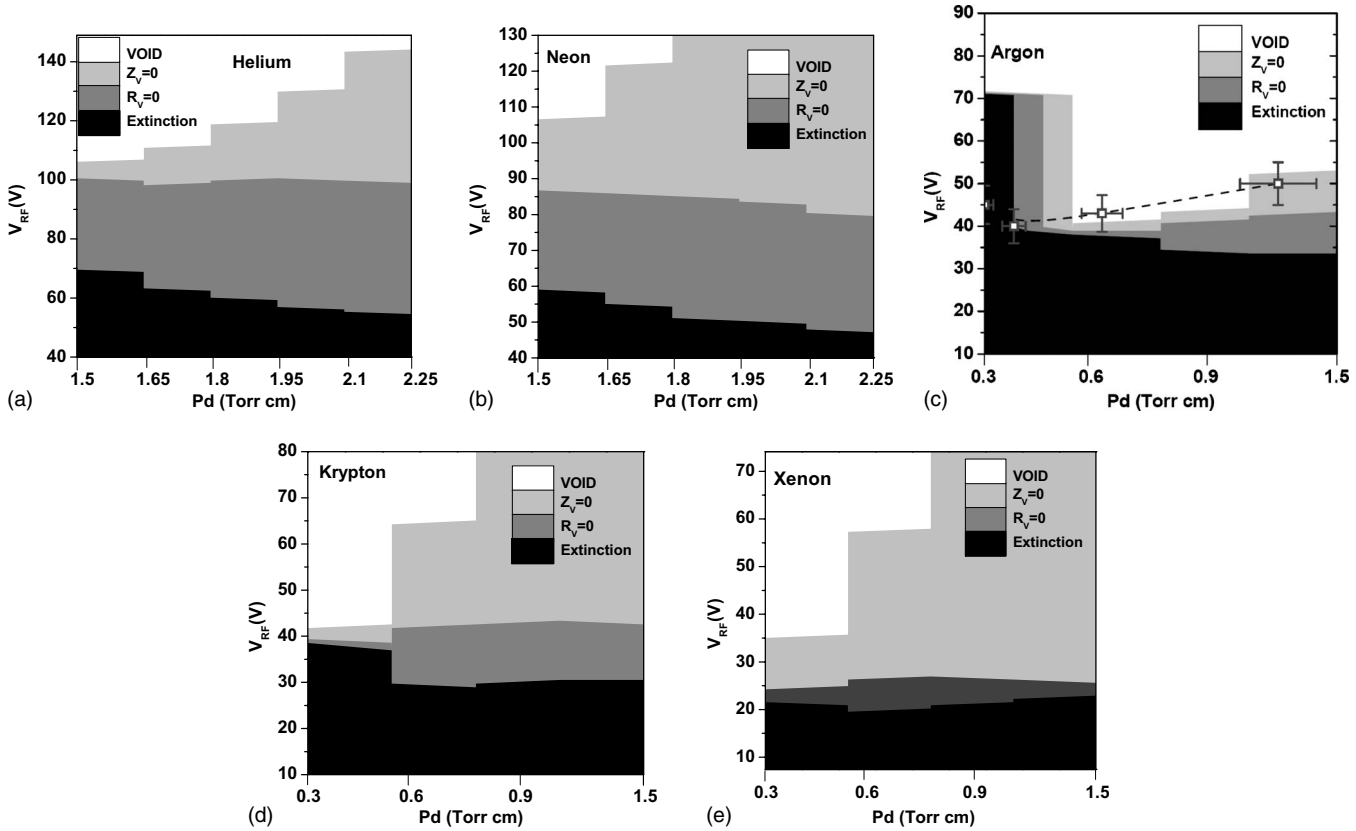

FIG. 7. $V_{rf}-Pd$ maps showing the different states of the dusty plasma under microgravity. The additional data in the argon plot represents experimental measurements of the breakdown voltage adapted from [42]. Data are obtained from a log-log plot, hence the large error bars.

more rigid, since 0.2 V can make the difference between creation of plasma or extinction of plasma. Some effects that might shift these lines not included in the model are the onset of instabilities or waves and the effect of dust inertia.

The first of the three curves is the extinction curve, since below this line, the plasma cannot be maintained. This curve looks very similar to the Paschen curves obtained for the breakdown potential in low-pressure discharges, but in rf discharges, such curves are more complicated than in Townsend-like discharges, as shown in [43,44]. The breakdown curve given for argon in [42] is similar to the model extinction curve [Fig. 7(c)], but also indicates not all physical processes are included. It is important to note that the rising part of any Paschen curve at low Pd is strongly determined by secondary electron emission processes, which we do not take into account in our model. Furthermore, at low pressures, collisionless electron-heating and nonlinear heating processes are required to explain how rf discharges can be maintained [45]. Such effects are not included here and are usually not included at all in fluid models, but require particle-in-cell and Monte Carlo approaches. This might be the reason why we cannot model helium and neon at low pressures even though dusty plasma experiments are performed in this range [17].

The second and third curves are the radial and axial void closure lines, below which the particles can freely move radially or axially towards the center of the discharge. All curves show similar dependence on driving potential, being properly fit by the same function, but with pressure-dependent factors that change with the type of gas. These two are determined by the forces acting on the dust and by how these forces depend on the driving potential and the pressure. We have shown that the thermophoretic force plays a minor role, promoting void closure axially, but preventing void closure radially. As such, the difference between the axial and radial void closure lines cannot be completely explained by thermophoresis alone.

Therefore, void closure is determined by the electrostatic force and ion drag. At the void edge, their ratio is close to 1. The ion drag is proportional to $n_+Q_d^2\boldsymbol{u}_+$ and the electrostatic force is given by $Q_d\mathbf{E}$. The local ion flow speed is low and the same both axially and radially [20]. Assuming that the ion flow is dominated by drift in the electric field, $\boldsymbol{u}_+=\mu_+\mathbf{E}$, the ratio of the forces is $F_{id}/F_E \propto n_+\mu_+Q_D$. $\mu_+ \propto 1/P$, while n_+ scales roughly $\propto P$, even though this differs slightly among the gases as shown in Fig. 2. The force ratio depends on Pd through the dust charge only. Since the dust charge decreases with Pd through the slight decrease in the electron temperature as well as through the increased ion current, the outward force should decrease with Pd throughout the discharge and the void should be *easier* to close with increasing Pd. Therefore, the void should close at higher and higher V_{rf} with increasing Pd in both directions.

A difference between the axial and radial void closures can only be due to the discharge *geometry*. To understand void closure, we have to consider the two-dimensional geometry of the discharge. In our model, the void acts as a shape-preserving ellipsoid, with a much longer radial axis,

because of the large electrode size compared to the interelectrode distance. Since the rate of change of the void size is the same radially and axially (see Fig. 5), a larger decrease in the driving potential is required to close the void radially. Making the interelectrode spacing equal to the diameter of the electrode would make the void more spherical, causing the axial and radial void closure lines to look the same.

A discussion of the transport coefficients is in order. The available data in the literature are growing, but still sparse. Solvers such as BOLSIG+ can be easily found, the main concern being how up-to-date the collision cross sections are. Not all inelastic collisions are included, but the most probable collisions are. Solvers for heavy particles are rare, but some are being developed [46]. A negative view could be that plasma modeling will never completely approach reality, since the transport coefficients and energy losses will never be completely known. On the other hand, a positive approach would state that performing experiments, such as void closure in our case, can be used to fine tune simulation models and reduce the error introduced by transport data. Furthermore, nonlocal effects, more specifically nonlocal electron heating due to the large mean-free path of electrons in low-pressure discharges, might play an important role. Monte Carlo plus particle-in-cell models and hybrid approaches are needed for further investigation, especially at low pressures. For the same reason, secondary electron emission is a process that cannot be readily included in an approach purely based on fluid models.

In conclusion, we have extended a complex plasma fluid model to include all noble gases. We simulated void closure over a wide range of pressures and powers for helium, neon, argon, krypton, and xenon and produced maps of driving potential-pressure space, showing where complex plasmas under microgravity conditions contain a void or are void-free. A fit that describes the void closure lines has been presented and it has been shown that void closure depends on the geometry of the discharge. Thermophoresis plays a secondary effect in void closure, opposing void closure radially and enhancing it axially. Continuously updating transport coefficients and finding analytic forms for the nonlinear electron heating source term and secondary electron emission terms are obvious areas where the model can be improved.

ACKNOWLEDGMENTS

This work was supported by NSF under Grant No. PHY-0648869 and CAREER Grant No. PHY-0847127. The authors appreciate the hard work by Mike Hutcheson to keep the computational clusters up and running.

[1] J. H. Chu and L. I, Phys. Rev. Lett. **72**, 4009 (1994).
[2] H. Thomas, G. E. Morfill, V. Demmel, J. Goree, B. Feuerbacher, and D. Möhlmann, Phys. Rev. Lett. **73**, 652 (1994).
[3] A. Melzer, T. Trottenberg, and A. Piel, Phys. Lett. A **191**, 301 (1994).
[4] Y. Hayashi and K. Tachibana, Jpn. J. Appl. Phys. **33**, L804 (1994).
[5] T. Ott, M. Bonitz, Z. Donkó, and P. Hartmann, Phys. Rev. E **78**, 026409 (2008).
[6] L.-J. Hou, Z. L. Mišković, A. Piel, and M. S. Murillo, Phys. Rev. E **79**, 046412 (2009).
[7] D. Samsonov, S. K. Zhdanov, R. A. Quinn, S. I. Popel, and G. E. Morfill, Phys. Rev. Lett. **92**, 255004 (2004).
[8] T. Sheridan, Phys. Plasmas **15**, 103702 (2008).
[9] G. E. Morfill, H. M. Thomas, U. Konopka, H. Rothermel, M. Zuzic, A. Ivlev, and J. Goree, Phys. Rev. Lett. **83**, 1598 (1999).
[10] O. S. Vaulina, A. P. Nefedov, O. F. Petrov, and V. E. Fortov, Phys. Rev. Lett. **88**, 035001 (2002).
[11] A. P. Nefedov, G. E. Morfill, V. E. Fortov, H. M. Thomas, H. Rothermel, T. Hagl, A. V. Ivlev, M. Zuzic, B. A. Klumov, A. M. Lipaev, V. I. Molotkov, O. F. Petrov, Y. P. Gidzenko, S. K. Krikalev, W. Shepherd, A. I. Ivanov, M. Roth, H. Binnenbruck, J. A. Goree, and Y. P. Semenov, New J. Phys. **5**, 33 (2003).
[12] D. Samsonov and J. Goree, Phys. Rev. E **59**, 1047 (1999).
[13] H. Rothermel, T. Hagl, G. E. Morfill, M. H. Thoma, and H. M. Thomas, Phys. Rev. Lett. **89**, 175001 (2002).
[14] S. A. Khrapak, A. V. Ivlev, G. E. Morfill, and H. M. Thomas, Phys. Rev. E **66**, 046414 (2002).
[15] A. M. Lipaev, S. A. Khrapak, V. I. Molotkov, G. E. Morfill, V. E. Fortov, A. V. Ivlev, H. M. Thomas, A. G. Khrapak, V. N. Naumkin, A. I. Ivanov, S. E. Tretschev, and G. I. Padalka, Phys. Rev. Lett. **98**, 265006 (2007).
[16] W. J. Goedheer, V. Land, and J. Venema, J. Phys. D **42**, 194015 (2009).
[17] M. Schwabe S. K. Zhadov H. M. Thomas, A. V. Ivlev, M. Rubin-Zuzic, G. E. Morfill, V. I. Molotkov, A. M. Lipaev, V. E. Fortov, and T. Reiter, New J. Phys. **10**, 033037 (2008).
[18] J. C. Adam, J. P. Boeuf, N. Dubuit, M. Dudeck, L. Garrigues, D. Gresillon, A. Heron, G. J. M. Hagelaar, V. Kulaev, N. Lemoine, S. Mazouffre, J. Perez Luna, V. Pisarev, and S. Tsikata, Plasma Phys. Controlled Fusion **50**, 124041 (2008).
[19] V. Land, W. J. Goedheer, and M. R. Akdim, Phys. Rev. E **72**, 046403 (2005).
[20] V. Land and W. J. Goedheer, New J. Phys. **8**, 8 (2006).
[21] W. J. Goedheer and V. Land, Plasma Phys. Controlled Fusion **50**, 124022 (2008).
[22] V. Land, E. Shen, B. Smith, L. Matthews, and T. Hyde, New J. Phys. **11**, 063024 (2009).
[23] A. D. Richards, B. E. Thompson, and H. H. Sawin, Appl. Phys. Lett. **50**, 492 (1987).
[24] G. J. M. Hagelaar and L. C. Pitchford, Plasma Sources Sci. Technol. **14**, 722 (2005).
[25] G. K. Grubert, M. M. Becker, and D. Loffhagen, Phys. Rev. E **80**, 036405 (2009).
[26] A. Bogaerts, M. Yan, R. Gijbels, and W. Goedheer, J. Appl. Phys. **86**, 2990 (1999).
[27] J. P. Boeuf and L. C. Pitchford, Phys. Rev. E **51**, 1376 (1995).
[28] L. S. Frost, Phys. Rev. **105**, 354 (1957).

[29] H. Helm, J. Phys. B **9**, 2931 (1976).
[30] H. W. Ellis, M. G. Thackston, E. W. McDaniel, and E. A. Mason, At. Data Nucl. Data Tables **31**, 113 (1984).
[31] L. A. Viehland and E. A. Mason, At. Data Nucl. Data Tables **60**, 37 (1995).
[32] A. Agrawal and S. V. Prabhu, J. Vac. Sci. Technol. A **26**, 634 (2008).
[33] *CRC Handbook of Chemistry and Physics*, 89th ed., edited by D. R. Lide (CRC Press, Cleveland, 2008).
[34] J. E. Allen, Phys. Scr. **45**, 497 (1992).
[35] S. A. Khrapak, S. V. Ratynskaia, A. V. Zobnin, A. D. Usachev, V. V. Yaroshenko, M. H. Thoma, M. Kretschmer, H. Höfner, G. E. Morfill, O. F. Petrov, and V. E. Fortov, Phys. Rev. E **72**, 016406 (2005).
[36] I. H. Hutchinson, Plasma Phys. Controlled Fusion **48**, 185 (2006).
[37] A. V. Ivlev, S. K. Zhdanov, S. A. Khrapak, and G. E. Morfill, Phys. Rev. E **71**, 016405 (2005).
[38] G. Gozadinos, A. V. Ivlev, and J. P. Boeuf, New J. Phys. **5**, 32 (2003).
[39] M. Lieberman and A. Lichtenberg, *Principles of Plasma Discharges and Materials Processing* (Wiley-Interscience, New York, 1994).
[40] F. Paschen, Ann. Phys. **273**, 69 (1889).
[41] O. Arp, D. Block, M. Klindworth, and A. Piel, Phys. Plasmas **12**, 122102 (2005).
[42] M. Radmilović-Radjenović and B. Radjenović, Plasma Sources Sci. Technol. **15**, 1 (2006).
[43] M. Radmilović-Radjenović and J. K. Lee, Phys. Plasmas **12**, 063501 (2005).
[44] I. Iliev, S. Gocheva-Ilieva, and N. Sabotinov, J. Optoelectron. Adv. Mater. **11**, 1392 (2009).
[45] G. Gozadinos, D. Vender, M. M. Turner, and M. A. Lieberman, Plasma Sources Sci. Technol. **10**, 117 (2001).
[46] T. K. Senega and R. P. Brinkmann, IEEE Trans. Plasma Sci. **35**, 1196 (2007).